Available online at www.sciencedirect.com
SCIENCE DIRECT®
International Journal of Heat and Fluid Flow 25 (2004) 22–31
International Journal of HEAT AND FLUID FLOW
www.elsevier.com/locate/ijhff

Numerical studies of heat transfer enhancements in laminar separated flows

Yongmann M. Chung *, Paul G. Tucker

Fluid Dynamics Research Centre, Department of Engineering, University of Warwick, Coventry CV4 7AL, UK

Received 17 March 2003; accepted 15 August 2003

Abstract

Numerical studies of unsteady heat transfer enhancements in grooved channel and sharp 180° bend flows of especial relevance to electronic systems are made. Prior to these, to find the most efficient numerical approaches, performances of various pressure correction, convective and temporal schemes are studied. To do this, the spatial development of an instability wave in a plane channel flow is modelled. Grooved channel flow predictions suggest a commonly used periodic flow assumption (for modelling rows of similar electronic components) may not always be valid over a significant system extent. For the bend flow, heat transfer enhancements due to passive and active control are considered. For the former, a thin tripping fin is attached at several inlet channel locations. If the fin is sufficiently high and far from the sharp bend edge, the flow becomes unsteady. Then, large-scale vortices emanating from the sharp edge cause a reduction in re-attachment length and a dramatic heat transfer enhancement. Active flow control is also studied for several inlet amplitudes and forcing frequencies. Like the passive fin, this active approach is effective at increasing heat transfer.

Keywords: Heat transfer enhancement; Finned surfaces; Sharp 180° bend; Grooved channel; Oscillatory flow

1. Introduction

With increasing power densities, the reliable computation of fluid flow and heat transfer in electronic systems is becoming ever more important (Kordyban, 1998; Chung et al., 2002). For electronic systems the Reynolds number (Re) range is typically $100 < Re < 5000$. Also, the geometry is generally complex with many corners, recesses, and regions where flows are sharply turned. Reynolds numbers can vary significantly in different regions of a single system. All of the above make the potential for the excitement of an oscillatory flow relatively high (Tucker, 2001). An extensive review of the application of computational fluid dynamics (CFD) to electronics is given by Tucker (1997). This shows that generally low accuracy numerical schemes are used and solutions assumed steady.

The exception to the above is the pioneering work of Ghaddar et al. (1986a) who study idealised two-dimensional isothermal cyclic flow in channels with integrated circuit (IC) like protrusions. The geometry considered is shown in Fig. 1(b). For Reynolds numbers less than a critical value Re_c the flow is found to be steady. Then, there is little transport of fluid between the main through flow and the groove area formed between the IC components. The flow undergoes a supercritical regular Hopf bifurcation at $Re = Re_c$. For $Re > Re_c$, cyclic flow oscillations which increase fluid transport to and from the groove are observed. Amon and Patera (1989) find that the secondary instability in the grooved channel flow is of narrow-band nature and very different from that in the plane channel flow.

Ghaddar et al. (1986b) and Patera and Mikic (1986) use two-dimensional non-isothermal predictions to illustrate the potential for naturally enhancing heat transfer using the unsteadiness observed by Ghaddar et al. (1986a). Amon and Mikic (1990) and Amon (1992) extend the above work, comparing heat transfer enhancement for flows where oscillations are induced

* Corresponding author. Tel.: +44-24-7657-4367; fax: +44-24-7641-8922.
E-mail address: y.m.chung@warwick.ac.uk (Y.M. Chung).

0142-727X/$ - see front matter © 2003 Elsevier Inc. All rights reserved.
doi:10.1016/j.ijheatfluidflow.2003.08.004

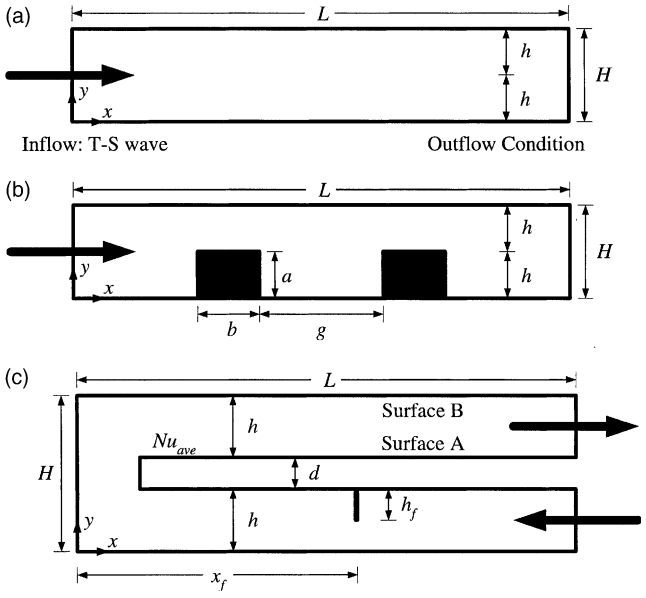

Fig. 1. Problem definition and computational domain: (a) plane channel, (b) grooved channel and (c) sharp bend flow.

passively by tripping, actively by flow modulation and naturally when $Re > Re_c$. Overall, when pumping losses are taken into consideration, passive heat transfer enhancement is found to be most effective. The above work uses a spectral element method (see Patera, 1984; Amon, 1993). The accuracy of this is initially demonstrated in Ghaddar et al. (1986a)'s grooved channel work by considering spatial development of a Tollmien–Schlichting (T–S) instability wave in plane channel flow (see Fig. 1(a)). This flow is linearly stable up to $Re_c = 5772$ (Orszag, 1971) (based on the half-channel height and the centre-line velocity). For $Re < Re_c$, instability shows a downstream decay.

Importantly, all of the above grooved channel work assumes periodic flow. However, the question still remains unanswered as to how realistic this assumption is in a practical electronics design context (i.e., over what percentage of a circuit board is the periodic flow assumption valid). Exploring this is an objective of the present work.

Chung et al. (2003) study the low Reynolds flow round a sharp 180° bend (see Fig. 1(c)). This is a prototype for flow sharply turned around circuit boards and is also found in the electronics cooling paper of Chung et al. (2001). Chung et al. (2003) show that for $Re > 600$ the flow becomes unsteady. Then, as in the grooved channel (1986a) dramatic increases in heat transfer are found. Following the path of Ghaddar et al. (1986a) here, this sharp bend flow work is extended by considering the use of active (by flow rate modulation) and passive (by a thin fin) flow control.

Such an exploration potentially requires a large volume of high fidelity (the flow physics is numerically challenging) numerical simulations. These need to consider, for example, different forcing frequencies, amplitudes and fin geometries in combination with different Reynolds numbers. Hence, efficient numerical approaches are required. Therefore, as part of this work initially the numerical performances of four pressure correction, eight convective and four temporal schemes are studied. To do this the spatial development of a T–S wave in plane channel flow is modelled. As noted earlier, this case is also considered by Ghaddar et al. (1986a). Since most practical electronic geometries are highly complex, numerical approaches that will most readily extend to such geometries are favoured. Although the present work is heavily motivated by electronics it also has strong relevance to other lower Reynolds number ventilation cases.

2. Problem formulations

As noted in Section 1, the geometries considered are: (I) a plane channel supporting a small amplitude instability wave; (II) a grooved channel with shear layer instability and (III) a sharp 180° bend with mostly a single thin fin. Case (I) is intended to help study efficiencies of various numerical schemes. Case (II) explores the validity of the periodic flow assumption commonly used in grooved channels. Case (III) is a prototype for flow sharply turned around circuit boards.

2.1. Case (I): Channel flow with T–S wave

For Case (I), shown in Fig. 1(a), plane Poiseuille flow having an exact analytic solution is considered (Chung et al., 1997). The temporal and spatial accuracy of various numerical schemes is verified by simulating the spatial development of an instability wave in Fig. 1(a) laminar channel flow. For theoretical investigations of travelling T–S wave instabilities, the plane Poiseuille flow can be regarded as a prototype case. This is because unlike the Blasius boundary layer flow, the base flow is strictly parallel and has an exact solution of the Navier–Stokes equations (Kleiser and Zang, 1991).

A T–S wave is obtained from eigensolution of the Orr–Sommerfeld equation. After Navier–Stokes equation linearisation and assuming a wave-like solution, the resulting Orr–Sommerfeld equation can be written as:

$$\left[(U_0 - \omega_R/\alpha)\left(\frac{d^2}{dy^2} - \alpha^2\right) - \frac{d^2}{dy^2}U_0 + \frac{i}{\alpha Re}\left(\frac{d^2}{dy^2} - \alpha^2\right)^2\right]\hat{v} = 0. \quad (1)$$

Here, U_0 is a base flow of the form $U_0(y) = y(2h - y)$. Also, α is the complex wave number $\alpha = \alpha_R + i\alpha_I$ and ω_R

the real frequency. The variables α_R and ω_R are related by the expression, $c = \omega_R/\alpha_R$. After obtaining $\hat{v}$ from Eq. (1), $\hat{u}$ can be easily calculated via the continuity equation, $\hat{u} = i\hat{v}/\alpha$.

The Reynolds number is defined as $Re = U_c h/v$, where U_c is the centre-line velocity, h the half-channel height and v the kinematic viscosity. Here $Re = 5000$ and the streamwise length of the computational domain is $50h$—approximately 10 times the T–S wave length.

2.2. Case (II): Grooved channel flow

For Fig. 1(b) grooved channel, $Re = 500$ (the Re definition is as for Case (I)). Also, for the groove forming blocks $a/h = 1$ and $b/h = 2$. The groove gap is $g/h = 8$. The first block is located at $x = 10$ (i.e., the upstream side of the block is located at $x = 10$ and the downstream at $x = 12$).

2.3. Case (III): Sharp 180° bend flow

For Fig. 1(c) bend flow, the channel height is h and the plate thickness d. In order to investigate the downstream flow recovery after the bend, the computational domain is long, $L = 20h$. Also, $d/h = 0.1$ is chosen as representative of a typical electronics system value. The Reynolds number is defined as $Re = U_m h/v$, where U_m is the bulk-mean velocity.

A thin highly-conductive fin can be located at five different axial positions (x_f) on the upper wall of the inlet channel. To investigate the effect of the fin length h_f, solutions with $h_f = 0.2h$, $0.3h$ and $0.4h$ are made.

3. Numerical methods

3.1. Governing equations

We consider two-dimensional unsteady laminar flows. The unsteady Navier–Stokes and continuity equations can be written in the following non-dimensional incompressible flow form:

$$\frac{\partial u_i}{\partial x_i} = 0, \tag{2}$$

$$\frac{\partial u_i}{\partial t} + \frac{\partial}{\partial x_j}\left(u_i u_j\right) = -\frac{\partial p}{\partial x_i} + v\frac{\partial^2 u_i}{\partial x_j^2}, \tag{3}$$

$$\frac{\partial T}{\partial t} + \frac{\partial T u_i}{\partial x_i} = -\frac{k}{\rho C_p}\frac{\partial^2 T}{\partial x_i^2}. \tag{4}$$

In the above, u_i is the instantaneous velocity in the x_i direction, p is the pressure, and T temperature. Here ρ is the fluid density, k thermal conductivity and C_p the specific heat capacity.

The governing equations are solved using a staggered grid finite volume method as implemented in the NEAT code (Tucker, 2001). Several, spatial discretisation, time-advancement and pressure correction algorithms are available in NEAT. Here the following spatial differencing schemes are tested (see Appendix A): first-order upwind; second-order upwind; third-order upwind (QUICK (Leonard, 1979)); second-order central differencing, Leith's scheme (see Leonard, 1979), Fromm (1970)'s model and CONDIF (Runchal, 1987). CONDIF is a stabilised second-order central differencing scheme. For temporal differencing the following are tested: first-order implicit backwards Euler; first-order forwards Euler, ADI and Crank–Nicholson. To gain a pressure field consistent with mass conservation the following are tested: SIMPLE (Patankar and Spalding, 1972), SIMPLEC (Van Doormaal and Raithby, 1984) (as formulated in Tucker, 2001), AVPI (Jones and Marquis, 1985), PISO (Issa, 1985) and a fractional step method (Choi and Moin, 1994). Full details of the above can be found in Tucker (2001) and Chung et al. (2003).

3.2. Boundary conditions

For all cases, parabolic inlet velocity profiles are used. For Case (I), a two-dimensional TS wave is superimposed on a laminar parabolic profile:

$$u_i'(x = 0, y, t) = A_{TS}\Re\left[\hat{u}_i(y)e^{-i\omega_R t}\right]. \tag{5}$$

A_{TS} is the amplitude of the inflow perturbations ($A_{TS} \ll 1$) and $\hat{u}_i(y)$ is the complex velocity vector. This is calculated from the spatial eigenfunctions of the Orr–Sommerfeld equation corresponding to the real frequency ω_R. $\Re$ represents the real part of a complex number. The amplitude of inflow disturbance $A_{TS} = 10^{-3}$ is defined as the root-mean-square (rms) magnitude of the T–S wave u component. The parabolic velocity profile for a plane channel is also used to set the initial flow condition. More details of the implementation of the inflow boundary condition can be found in Chung et al. (1997).

At outflow boundaries, to suppress wave reflections the following convective boundary condition (Pauley et al., 1990) is applied

$$\frac{\partial u_i}{\partial t} + U_{conv}\frac{\partial u_i}{\partial x} = 0, \tag{6}$$

where $U_{conv} = U_m$ characterises the convective exit velocity. At solid walls, the no-slip and impermeability conditions are applied.

Cases (I) and (II) are isothermal. For Case (III), the temperature of the incoming flow is constant at T_i. The temperature of the wall, located at $y = h + d$, after the bend (Surface A) is T_w. For relevance to heat transfer from circuit boards $T_w > T_i$ and the upper wall

(Surface B), located at $y = H$, is adiabatic. The temperature at the remaining walls is constant at T_i.

3.3. Numerical parameters

For all cases, wall-normal hyperbolic-tangent function grid stretching is implemented. For cases (I)–(III), to give grid independent solutions, the $(x \times y)$ grid node numbers are 512×129, 1046×65 and 569×143, respectively. For time step (Δt) independent solutions, the following are used: $\Delta t = 0.05$, 0.05 and 0.01 for cases (I)–(III), respectively.

4. Results and discussion

4.1. Channel flow with T–S wave

A standard case is chosen carefully from Chung et al. (1997). Initially in both the convective and diffusive terms, the Crank–Nicholson and second-order central difference (CD2) schemes are used.

Fig. 2 gives T–S waves disturbance streamfunction contours. Broken lines represent negative values of the streamfunction. To describe the accuracy of various schemes quantitatively, it is useful to measure the spatial growth of disturbances. Several different criteria for measuring the disturbance amplitude have been devised in the literature. Among them, the following disturbance kinetic energy $E(x)$ has been adopted here:

$$E^2(x) = \frac{1}{2}\int_0^2 \left[\overline{u'^2}(x,y) + \overline{v'^2}(x,y)\right] \mathrm{d}y. \tag{7}$$

Here, $\overline{(\ )}$ represents time averaging. The analytic disturbance kinetic energy decays as $e^{-\alpha_I t}$ with a rate $\alpha_I = 0.0106$ and a wave number $\alpha_R = 1.1557$ (Orszag, 1971). The predicted α_I is 0.0109.

4.1.1. Discretisation schemes

Now, the effects of discretisation schemes on the wave number α_R and the decay rate constant α_I are explored. Schemes with dispersion error will affect α_R. Those with false diffusion affect the decay rate constant α_I. Fig. 3 shows the choice of spatial differencing scheme has a strong influence on the solution. The decay in the first-order upwind (UP) and hybrid (HYB) schemes is unacceptable. Among others, the second-order central difference (CD2) scheme performs well. Compared to the other schemes tested the errors both in the wave number α_R and the decay rate constant α_I are insignificant.

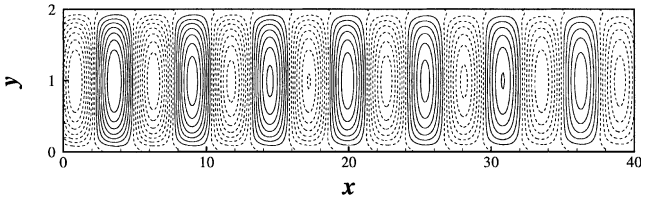

Fig. 2. Plot of x–y plane disturbance streamfunction.

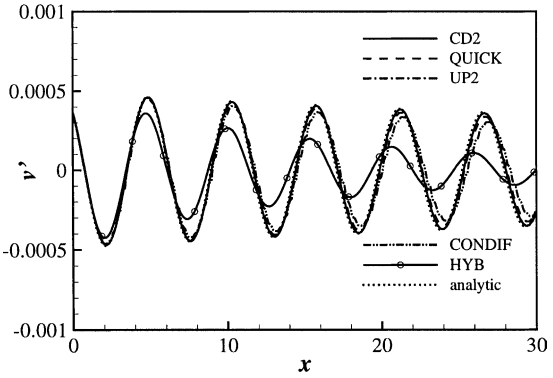

Fig. 3. Comparison of various discretisation schemes.

These errors and the efficiency of each scheme are compared with analytic solution in Table 1. QUICK, second-order upwind (UP2) and Fromm's scheme have virtually identical efficiencies to CD2. Lower-order scheme accuracies (UP and HYB) are poor for the decay rate constant α_I. However, the wave number α_R errors are reasonable (<2.5%). When schemes with a substantial decay rate α_I error are used to simulate complex flows, the strength of flow structures is substantially underestimated. In a complex flow, with more than one dominant frequency, the flow structure strength may change the flow's frequency characteristics.

CONDIF has a small error in the wave number α_R, but the decay rate constant α_I error is 60%. A key CONDIF feature found here is relatively poor convergence and hence the need for about five times more computing time. However, at higher Reynolds numbers with practical grids, CD2 can become virtually impossible to converge. CONDIF then becomes more attractive. Although QUICK and UP2 here show similar performances to CD2, for more complex flows their relatively low order upwind natures can contaminate turbulence energy spectra (Kravchenko and Moin, 2000). Therefore, a conclusion here is that for lower Re flows the more computationally economical, easier to

Table 1
Discretisation scheme errors compared to the analytic solution and efficiencies compared to the CD2 scheme

Scheme	$E(\alpha_R)$	$E(\alpha_I)$	Δ(Iteration)
CD2	−0.25	2.8	1.00
QUICK	−0.26	2.7	1.07
UP2	−0.32	2.6	1.12
CONDIF	−1.3	65	5.54
HYB	2.2	440	0.93
UP	2.2	460	0.94

Here, $E(\phi) = (\phi - \phi_{exact})/\phi_{exact} \times 100$ and $\Delta(\phi) = \phi/\phi_{CD2}$. A 513×129 grid is used.

implement CD2 scheme is preferable and so is used for the main simulations.

4.1.2. Time-advancement methods

Use of the potentially faster explicit in time (and hence requiring estimated streaming terms) forms of CD2 and QUICK was explored. However, the explicit solutions are found too unstable. As expected, the more dissipative first-order implicit Euler method amplitude has about a 40% lower α_I than that for the Crank–Nicholson, ADI and analytic results. Computational time savings arising from improved first-order scheme stability are insufficient to compensate for the accuracy loss. For the present two-dimensional case, ADI, which gives virtually identical results to Crank–Nicholson, just requires a line solver and so is most efficient. However, partly since we hope to extend in the future Case (III) simulations to 3D, for the main simulations Crank–Nicholson is used.

4.1.3. Pressure algorithms

For pressure related algorithms, efficiency is the key comparison point. Simulations are performed over one T–S period when $t > 200$. Surprisingly, results show that for a broad range of convergence levels, efficiencies for all schemes are similar to within 10%. The fractional step method of Choi and Moin (1994) is also considered. The saving for this is certainly no more than 10%. Therefore, the lower storage AVPI scheme seems a sensible choice.

4.2. Grooved channel flow

Fig. 4(a) gives grooved channel instantaneous streamline contours. After the first block, the flow becomes unsteady. This increases with x and eventually, the unsteadiness fluctuations become the same order of magnitude as U_m. Fig. 4(b) highlights through C_f the downstream flow development. Note, for a fully developed plane channel flow $C_f = 2$. The strong C_f singularities at $x = 10$, 20, 30, 40, 50, 60 and 70 are caused by the sharp groove edges. For $x < 30$ the C_f profile changes substantially with x. The negative C_f peak has a fully developed value around the fifth groove. Fig. 4(c) plots fluctuating kinetic energy (k) against x. The measuring points are $3h$ downstream of each block and at $y/h = 1$. Consistent with the C_f evidence, after the fifth block, k reaches a quasi-fully developed value. After this $x > 50$ region, flow periodicity (Yang and Ferziger, 1993) could be assumed.

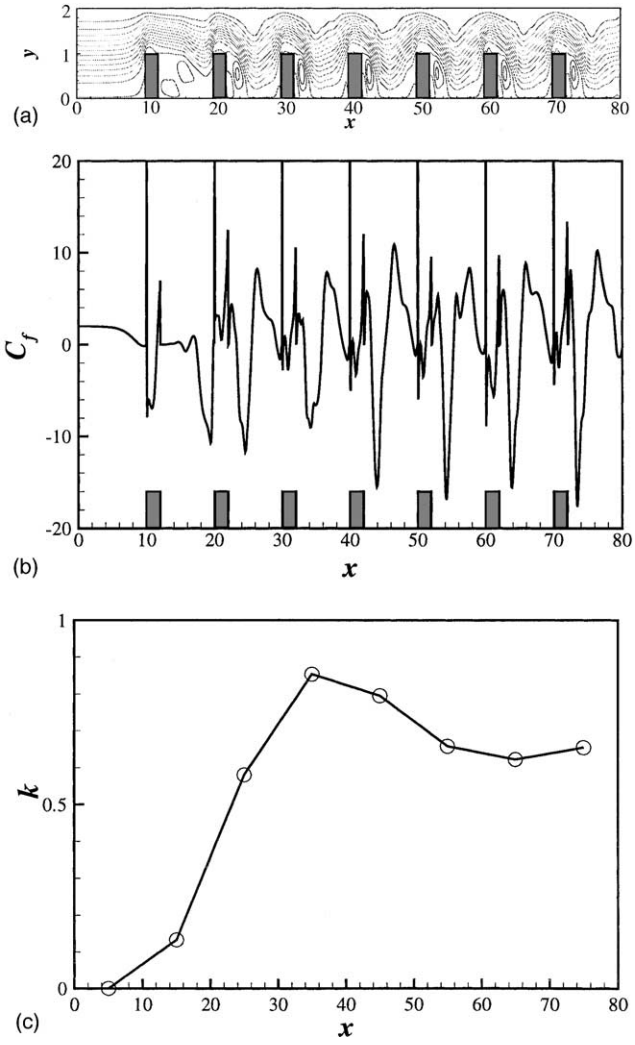

Fig. 4. Grooved channel flow: (a) streamlines, (b) C_f distributions and (c) rms of velocity fluctuations k at the recirculation zone.

4.3. Sharp bend flow

4.3.1. Flow and heat transfer without fins ($h_f = 0$)

Laminar flow and heat transfer simulations for a sharp bend flow without fins (i.e., a fin length $h_f = 0$) are performed in Chung et al. (2003). For $Re > 600$ the flow is found to become oscillatory. This is clear from Fig. 5, showing the velocity time history at the measuring point ($x = 20$, $y \approx 1.6$) for $Re = 500$ and 700. For $Re = 500$ (Fig. 5(a)), by $t > 60$ the flow is quasi-steady. However, with increasing Re, significant oscillations are sustained. The dominant low frequency component corresponds to vortex shedding from the sharp corner.

Fig. 6 shows the re-attachment length x_r and Nu_{ave} as a function of Re. The parameter x_r is the distance from the edge of the bend ($x = 1.0$) to where the time-mean velocity gradient (dU/dy) at Surface A is zero. To emphasise the effect of flow unsteadiness in the recirculation region, Nu is averaged over the $Re = 300$ recirculation region extent ($1 \leqslant x \leqslant 5$). It can be seen that, for steady flow ($Re < 600$) x_r increases with Re, and Nu stays relatively constant. Conversely, for unsteady flow ($Re > 600$) x_r is substantially reduced and Nu increases dramatically. For further thermofluid details of this $h_f = 0$ case, see Chung et al. (2003).

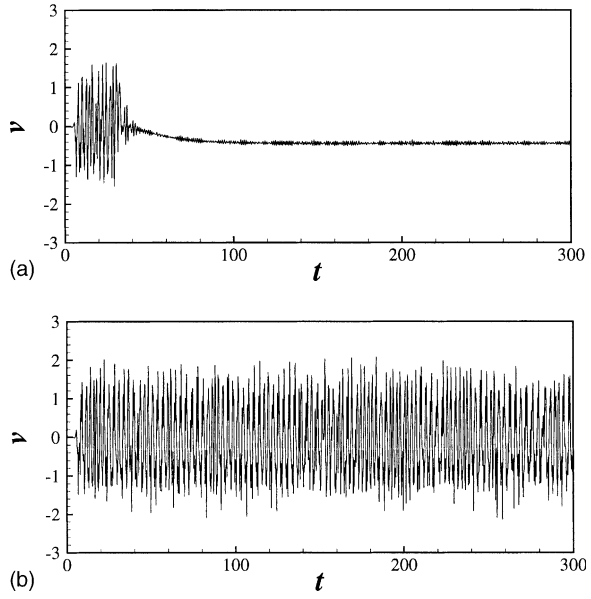

Fig. 5. Instantaneous v velocity at the measurement point ($x = 15$, $y = 1.6$): (a) $Re = 500$ and (b) $Re = 700$.

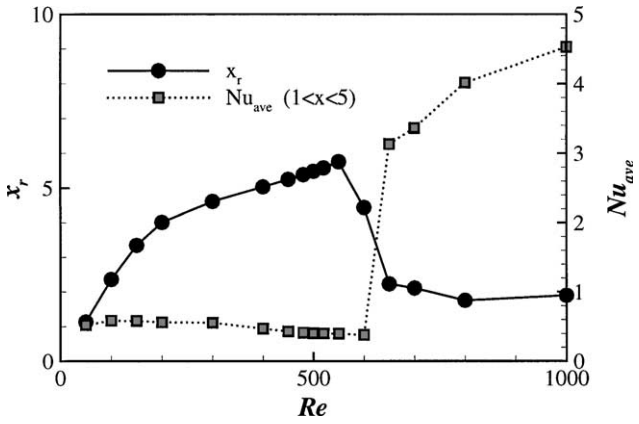

Fig. 6. Reattachment length x_r and Nu_{ave} as a function of Re.

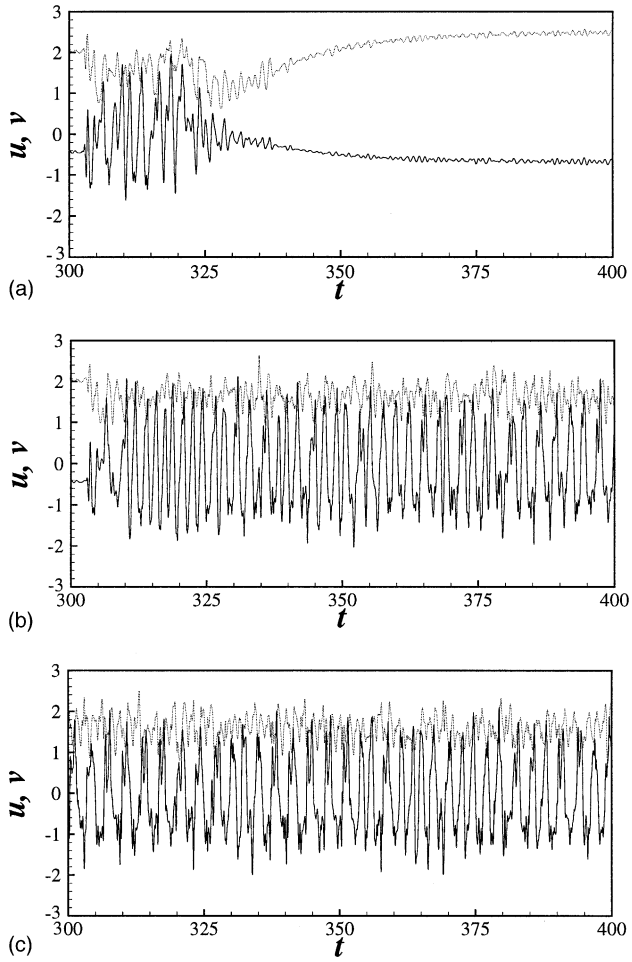

Fig. 7. Instantaneous u (dotted lines) and v (solid lines) velocities at the measurement point ($x = 15$, $y = 1.6$) for $Re = 500$ with $h_f = 0.3$: (a) $x_f = 2.0$, (b) $x_f = 5.0$ and (c) $Re = 700$, uncontrolled.

4.3.2. Flow with a thin fin

For cases with a fin, $Re = 500$. Initial conditions are those for Fig. 5(a) at $t = 300$. Fig. 7, like Fig. 5, gives velocity time histories at the measuring point. Fig. 7(a) shows that with a $h_f = 0.3$ fin near the bend edge ($x_f = 2.0$), the flow is quasi-steady. However, Fig. 7(b) suggests for $x_f \geqslant 3.0$ and $h_f = 0.3$ the flow becomes oscillatory. Fig. 7(b) traces indicate quasi-periodicity and look similar to those for $Re = 700$ and $h_f = 0$ shown in Fig. 7(c).

Fig. 8 shows instantaneous streamlines for two different Reynolds numbers, fin positions and heights. Fig. 8(a) and (b) shows that for $Re = 500$ with $h_f = 0$ and $h_f = 0.3$ but $x_f < 5$ the flow is steady. However, as can be seen from Fig. 8(c), for $x_f \geqslant 5.0$, large-scale vortices emanate from the sharp corner. These convect downstream with a velocity of about 60% of U_m. It is clear, when also studying Fig. 7(c), that the large-scale vortex shedding dominates the flow field. The amplitude of the flow oscillations decays slowly with downstream location. Comparison of Fig. 8(c) and (d) shows the passively controlled $Re = 500$ flow can be made similar to that for $Re = 700$.

It is evident that thin fin passive flow control significantly affects the mean flow field. Fig. 9 repeats Fig. 8 but this time giving time-mean velocity vectors more focused on the bend region. Fig. 9(b) flow is similar to that in Fig. 9(a) for $h_f = 0$. With a fin positioned at $x_f = 2.0$, the recirculation region flow is separated from the high velocity fluid external to it. Hence, there is minimal mixing between the two regions. With $x_f = 5.0$ and hence unsteadiness, the recirculation region size reduces dramatically from $x_r = 5.48$ (Fig. 9(a)) to $x_r = 2.18$ as shown in Fig. 9(c). With $x_f = 5.0$, there is strong mixing inside the recirculation zone and the maximum reverse velocity is of the same order as U_m. This is consistent with C_f data presented later. For

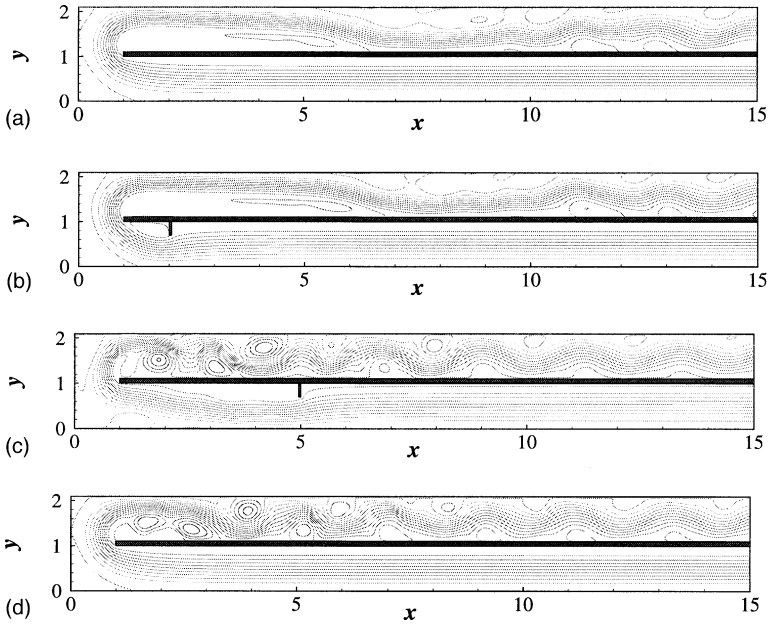

Fig. 8. Contours of instantaneous streamlines: (a) $Re = 500$, $h_f = 0$, (b) $Re = 500$, $x_f = 2.0$, $h_f = 0.3$, (c) $Re = 500$, $x_f = 5.0$, $h_f = 0.3$ and (d) $Re = 700$, $h_f = 0$. Increments are $\Delta\psi = 0.1$.

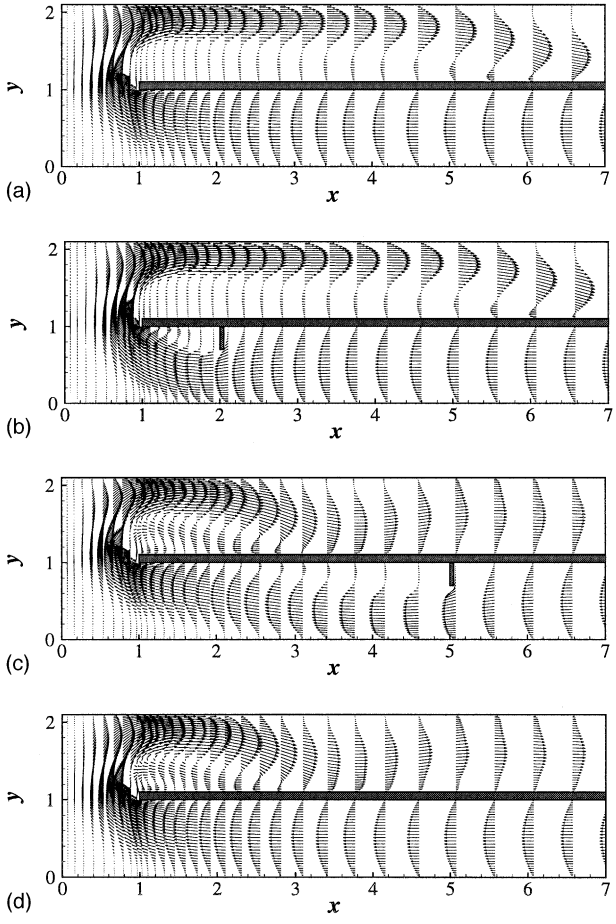

Fig. 9. Velocity vector plots of time-mean flow field: (a) $Re = 500$, $h_f = 0$, (b) $Re = 500$, $x_f = 2.0$, $h_f = 0.3$, (c) $Re = 500$, $x_f = 5.0$, $h_f = 0.3$ and (d) $Re = 700$, $h_f = 0$.

$x_f > 5.0$, the overall flow features do not change much looking similar to Fig. 9(d) $Re = 700$ flow.

To investigate the effect of a fin on the onset of flow unsteadiness, the velocity fluctuations u_{rms} and v_{rms} are analysed for $x_f = 5.0$ and $h_f = 0.3$. Fig. 10(a) gives contours of v_{rms}. Velocity fluctuation profiles at $y = 0.7$ are shown in Fig. 10(b). Note that the horizontal axis is the distance away from the fin, $x_f - x$. It is clear from the figure that, as the flow passes the fin, the velocity fluctuations grow exponentially up to about 1% of the mean velocity at $x = 3.0$. Then, the fluctuations remain relatively constant until the flow reaches the bend edge ($x = 1.0$). With a fin located closer to the bend edge ($x_f \leqslant 3.0$), u_{rms} and v_{rms} do not significantly grow. Without a fin, the velocity fluctuations are orders of magnitude smaller and the flow remains steady (see Fig. 8).

Fig. 11 shows the C_f distributions at Surface A. It can be seen from the dashed and dotted lines that with a fin located close to the edge ($x_f \leqslant 3.0$) x_r does not significantly change. The dot-dashed line shows an abrupt change occurs for $x_f \geqslant 5.0$. The C_f distribution is then similar to that for $Re = 700$ (thick full line).

4.3.3. Heat transfer with a fin

Fig. 12 shows $h_f = 0.3$ time-mean Nusselt number ($Nu = \frac{h}{\Delta T}\frac{dT}{dy}$, where $\Delta T = T_w - T_i$) distributions along Surface A. Initially, Nu increases with x. Then, due to boundary layer development, it decreases. Analysis shows the maximum Nusselt number (Nu_{max}) occurs just downstream of the time-mean re-attachment points (Chung et al., 2003). Without a fin ($Re = 500$, thin full

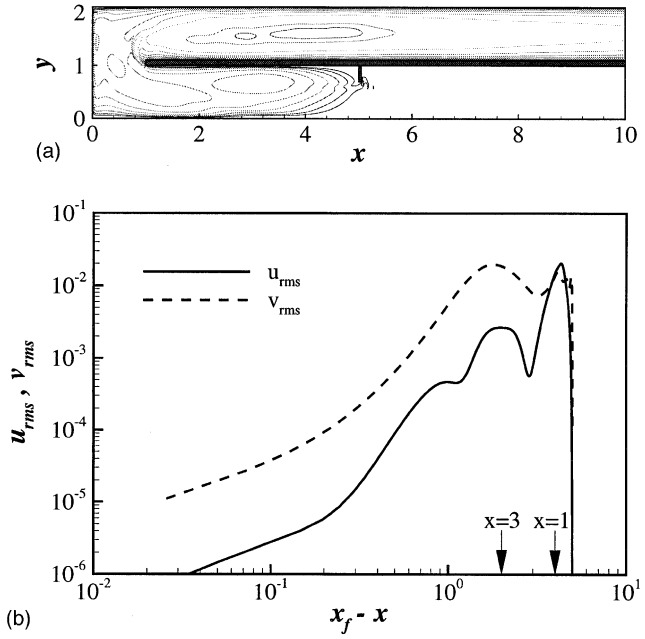

Fig. 10. $Re = 500$, $x_f = 5.0$ and $h_f = 0.3$: (a) v_{rms} contours and (b) u_{rms} and v_{rms} profiles at $y = 0.7$.

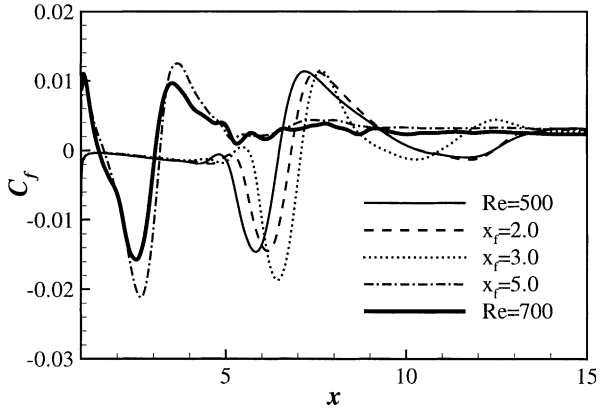

Fig. 11. C_f distributions along Surface A with $h_f = 0.3$.

line), Nu_{max} is nearly an order of magnitude larger than Nu in the recirculation zone. With a fin at $x_f \leqslant 3.0$, Nu does not change much from the uncontrolled $h_f = 0$ case. However, it is clear from the figure that, as the flow becomes oscillatory ($x_f \geqslant 5.0$), the Nu distribution shows similar trends to that for $Re = 700$ (thick full line). Nu is increased substantially and the Nu_{max} location suddenly moves upstream. Also, the $x < 5$ region where Nu is small ($Nu < 1$) almost disappears. These findings are consistent with Fig. 11 C_f distributions.

To investigate the effect of the fin length, x_r and Nu_{ave} are plotted against x_f in Fig. 13 for three fin lengths (see also Figs. 11 and 12). The data at $x_f = 0$ represents the cases without a fin. Fig. 13(a) and (b) gives x_r and Nu_{ave}, respectively. As can be seen, a short fin ($h_f = 0.2$) has

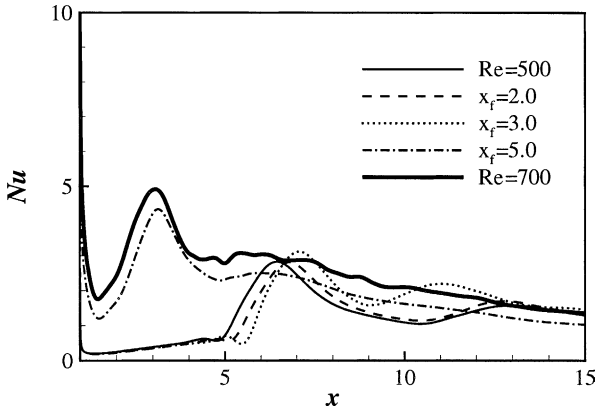

Fig. 12. Nu distributions along surface A with $h_f = 0.3$.

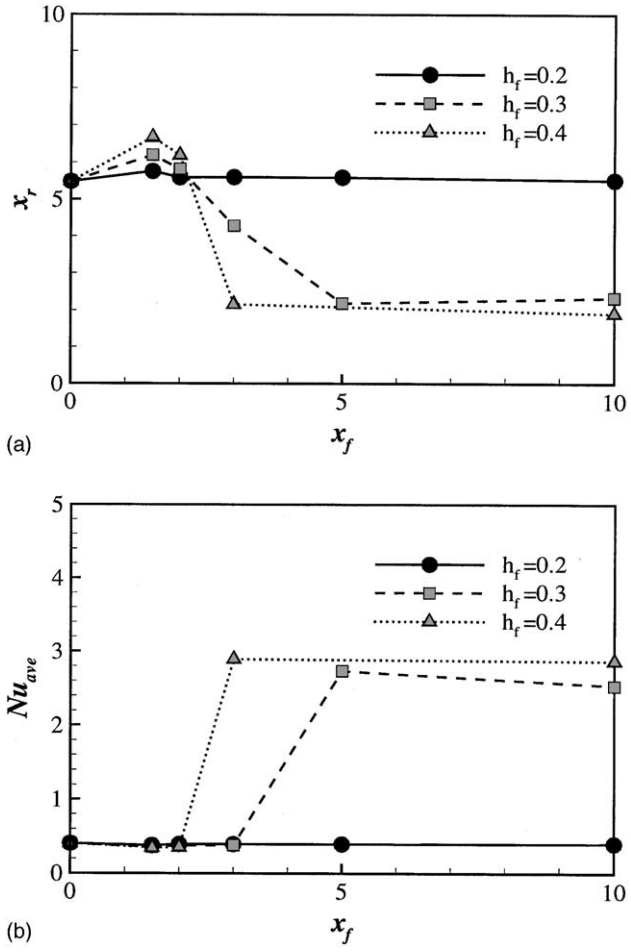

Fig. 13. x_r and Nu as a function of x_f.

little x_r and Nu_{ave} influence. However, for sufficiently large h_f and x_f, the consequences of unsteadiness are clear. The fin position (x_f) for the onset of unsteadiness decreases with h_f. For controlled cases, the reduction in x_r and Nu increase are clear.

To investigate the effect of flow unsteadiness on convective heat transfer, instantaneous data are analysed.

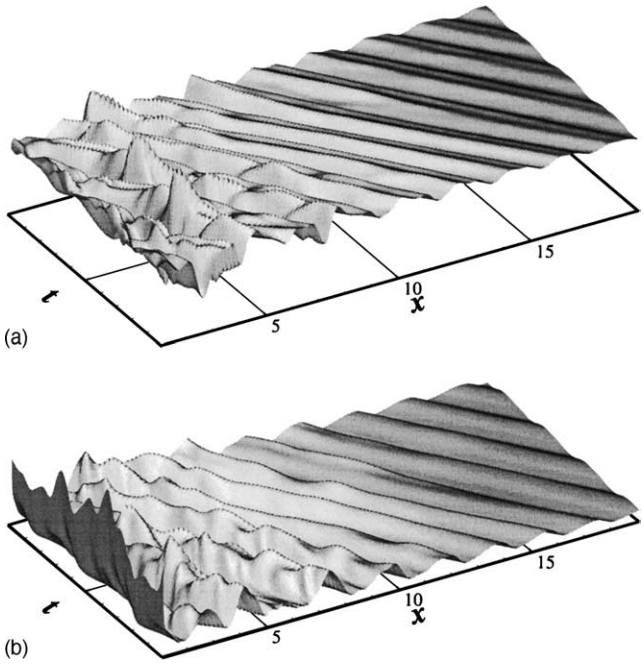

Fig. 14. Surface A space–time plots: (a) C_f and (b) Nu.

Fig. 14 gives space–time Surface A plots of C_f and Nu for $x_f = 5.0$ and $h_f = 0.3$. Oscillations (also evident in temperatures) due to the constant speed downstream propagation of large-scale vortices are evident. The oscillatory part of C_f and Nu is significant compared to the mean values. Also, the instantaneous Nu distribution correlates well with wall shear stress (Chung and Luo, 2002; Chung et al., 2002).

4.3.4. Effect of flow rate modulation

Simulations are again performed at the subcritical $Re = 500$, with sinusoidal inlet flow oscillations. First, the effect of the modulation amplitude (A) is considered. Fig. 15 plots x_r and Nu_{ave} against A. The forcing frequency $f = 0.5$. This corresponds to the $Re = 700$ natural frequency determined from instantaneous velocity data by Chung et al. (2003). Clearly the bend flow is sensitive to inlet flow oscillation. With just a 1.0% flow modulation, oscillatory flow and hence dramatic x_r decreases with Nu increases are gained. Above this oscillatory flow value, C_f and Nu distributions become insensitive to further increases in A.

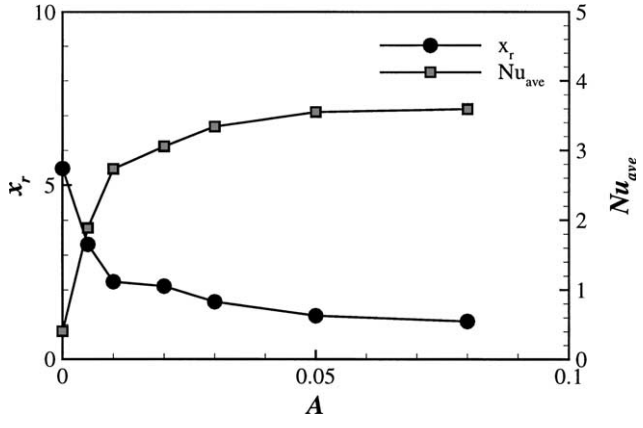

Fig. 15. x_r and Nu variations against amplitudes A with $f = 0.5$.

The harmonic forcing frequencies of $f = 1.0$ and 2.0 are also considered. For large amplitudes ($A \geqslant 0.02$), the flow is found unsteady for both frequencies. This unsteadiness again gives an x_r decrease and a significant Nu increase. Results suggest flow modulation is effective at increasing low Reynolds number heat transfer, especially when the pumping power is limited.

5. Conclusions

The accuracies of various numerical methods for unsteady low Re flow calculations are studied. Eight convective term spatial discretisation, four pressure prediction and four temporal schemes are considered. It is found that, relative to steady flow computations, the overall effects of pressure algorithms on efficiency are not that great. Therefore, here, the lower storage AVPI scheme was perhaps the most attractive. Results show lower-order schemes have a strong influence on both global flow structures and unsteadiness amplitudes. The numerically simple space and time centred, central difference and Crank–Nicholson schemes are shown to perform well. Indeed for the Reynolds numbers considered the central difference scheme has better overall efficiency than its stabilised CONDIF counterpart.

Unsteady laminar grooved channel flow predictions for $Re = 500$ show the flow becomes periodic by around

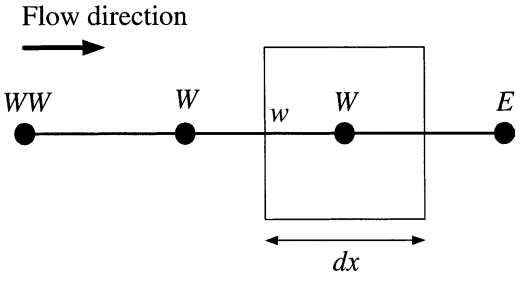

Fig. 16. Interpolation of flow variables to the 'w' face of a control volume.

Table 2
Weighting function values

Scheme	$W_{f_{WW}}$	W_{f_W}	W_{f_P}	HOT
UP	0	1	0	$\partial^2\phi/\partial x^2$
UP2	−1/2	3/2	0	$\partial^3\phi/\partial x^3$
CD2	0	1/2	1/2	$\partial^3\phi/\partial x^3$
QUICK	−1/8	6/8	3/8	$\partial^4\phi/\partial x^4$
HYB ($u\Delta x/\nu > 2$)	0	1	0	$\partial^2\phi/\partial x^2$
HYB ($u\Delta x/\nu \leqslant 2$)	0	1/2	1/2	$\partial^3\phi/\partial x^3$

Here, HOT means higher-order terms in the discretisation.

the fifth rib. Hence, when modelling IC rows on circuit boards the popular periodic flow assumption might not always be valid for a significant region.

Simulations of unsteady laminar flow around a sharp 180° bend with a thin fin of various heights, h_f and distances, x_f from the bend edge are performed. For sufficiently large x_f and h_f oscillatory flow is found. Oscillations cause a substantial reduction in the re-attachment length and a dramatic heat transfer increase. For a successful control case, the re-attachment length is reduced by more than half and the Nusselt number increases by over a factor of five. Active flow control, using flow rate modulation is also studied for several amplitudes and three forcing frequencies. Flow modulation, like thin fin tripping, appears to be effective at increasing electronics system related heat transfer, especially when the pumping power is limited.

Acknowledgements

The support of the Engineering and Physical Sciences Research Council (EPSRC) of the United Kingdom under grant number GR/N05581 is gratefully acknowledged.

Appendix A

In discretising convective terms, grid point values are interpolated to control volume face. For example, for a west 'w' control volume face, as shown in Fig. 16, (with a positive velocity component) the following interpolation expression can be used

$$\phi_w = W_{f_{WW}}\phi_{WW} + W_{f_W}\phi_W + W_{f_P}\phi_P. \quad (A.1)$$

The uniform grid weighting function values for the various convective schemes used here are given in Table 2.

References

Amon, C.H., 1992. Heat transfer enhancement by flow destabilization in electronic chip configurations. J. Electron. Packaging 114, 35–40.

Amon, C.H., 1993. Spectral element-Fourier method for transitional flows in complex geometries. AIAA J. 31 (1), 42–48.

Amon, C.H., Mikic, B.B., 1990. Numerical prediction of convective heat transfer in self-sustained oscillatory flows. J. Thermophys. 4 (2), 239–246.

Amon, C.H., Patera, A.T., 1989. Numerical calculation of stable three-dimensional tertiary states in grooved-channel flow. Phys. Fluids 1 (12), 2005–2009.

Choi, H., Moin, P., 1994. Effects of the computational time step on numerical solutions of turbulent flow. J. Comput. Phys. 113, 1–4.

Chung, Y.M., Luo, K.H., 2002. Unsteady heat transfer analysis of an impinging jet. ASME J. Heat Transfer 124, 1039–1048.

Chung, Y.M., Sung, H.J., Boiko, A.V., 1997. Spatial simulation of the instability of channel flow with local suction/blowing. Phys. Fluids 9 (11), 3258–3266.

Chung, Y.M., Tucker, P.G., Luo, K.H., 2001. Large-eddy simulation of complex internal flows. In: Geurts, B.J., Friedrich, R., Mètais, O. (Eds.), Direct and Large-Eddy Simulation IV. Kluwer Academic Publishers, The Netherlands, pp. 373–380.

Chung, Y.M., Luo, K.H., Sandham, N.D., 2002. Numerical study of momentum and heat transfer in unsteady impinging jets. Int. J. Heat Fluid Flow 23, 592–600.

Chung, Y.M., Tucker, P.G., Roychowdhury, D.G., 2003. Unsteady laminar flow and convective heat transfer in a sharp 180° bend. Int. J. Heat Fluid Flow 24, 67–76.

Fromm, J.E., 1970. A numerical study of buoyancy driven flows in room enclosures. In: 2nd Int. Conf. on Numerical Methods in Fluid Dynamics, University of California, USA, pp. 120–126.

Ghaddar, N.K., Karczak, K.Z., Mikic, B.B., Patera, A.T., 1986a. Numerical investigation of incompressible flow in grooved channels, Part1. Stability and self-sustained oscillations. J. Fluid Mech. 163, 99–127.

Ghaddar, N.K., Magen, M., Mikic, B.B., Patera, A.T., 1986b. Numerical investigation of incompressible flow in grooved channels, Part 2. Resonance and oscillatory heat-transfer enhancement. J. Fluid Mech. 168, 541–567.

Issa, R.I., 1985. Solution of the implicit discritized fluid flow equations by operator-splitting. J. Comput. Phys. 62, 40–65.

Jones, W.P., Marquis, A.J., 1985. Calculation of axisymmetric re-circulating flows with a second order turbulence model. In: Proc. Turbulent Shear Flows—5, Connel University, USA, p. 20.1.

Kleiser, L., Zang, T.A., 1991. Numerical simulation of transition in wall-bounded shear flows. Annu. Rev. Fluid Mech. 23, 495–537.

Kordyban, T., 1998. Hot Air Rises and Heat Sinks. ASME Press.

Kravchenko, A.G., Moin, P., 2000. Numerical studies of flow over a circular cylinder at $Re_D = 3900$. Phys. Fluids 12 (2), 403–417.

Leonard, B.P., 1979. A stable and accurate convective modelling procedure based on quadratic upwind interpolation. Comput. Methods Appl. Mech. Eng. 19, 59–99.

Orszag, S.A., 1971. Accurate solution of the Orr–Sommerfeld stability equation. J. Fluid Mech. 50, 689–703.

Patankar, S.V., Spalding, D.B., 1972. A calculation procedure for heat, mass and momentum transfer in three-dimensional parabolic flows. Int. J. Heat Mass Transfer 15, 1787–1806.

Patera, A.T., 1984. A spectral element method for fluid dynamics: laminar flow in a channel expansion. J. Comput. Phys. 54, 468–488.

Patera, A.T., Mikic, B.B., 1986. Exploiting hydrodynamic instabilities. Resonant heat transfer enhancement. Int. J. Heat Mass Transfer 29 (8), 1127–1138.

Pauley, L.R., Moin, P., Reynolds, W.C., 1990. The structure of two-dimensional separation. J. Fluid Mech. 220, 397–411.

Runchal, A.K., 1987. CONDIF: A modified central-difference scheme for convective flows. Int. J. Numer. Methods Eng. 24, 1593–1608.

Tucker, P.G., 1997. CFD applied to electronic systems: a review. Trans. IEEE (CPMTA) 20 (4), 518–529.

Tucker, P.G., 2001. Computation of unsteady internal flows. Kluwer Academic Publishers.

Van Doormaal, J.P., Raithby, G.D., 1984. Enhancements of the SIMPLE method for predicting incompressible fluid flows. Numer. Heat Transfer 7, 147–163.

Yang, K.S., Ferziger, J.H., 1993. Large-eddy simulation of turbulent obstacle flow using a dynamic subgrid-scale model. AIAA J. 31, 1406–1413.